Self-assembled highly ordered acid layers in precisely sulfonated polyethylene produce efficient proton transport

Edward B Trigg, Taylor W Gaines, Manuel Maréchal, Demi E Moed, Patrice Rannou, Kenneth B Wagener, Mark J Stevens, Karen I Winey

Self-assembled highly ordered acid layers in precisely sulfonated polyethylene produce efficient proton transport

Edward B. Trigg[1], Taylor W. Gaines[2], Manuel Maréchal[3], Demi E. Moed[1], Patrice Rannou[3], Kenneth B. Wagener[2], Mark J. Stevens[4], and Karen I. Winey[1]*

[1]Department of Materials Science and Engineering, University of Pennsylvania, Philadelphia, PA, USA.
[2]The George and Josephine Butler Polymer Research Laboratory, Department of Chemistry, University of Florida, Gainesville, FL, USA.
[3]Univ. Grenoble Alpes, CNRS, CEA, INAC-SyMMES, Grenoble, France.
[4]Center for Integrated Nanotechnologies, Sandia National Laboratories, Albuquerque, NM, USA.
*e-mail: winey@seas.upenn.edu

Abstract: Recent advances in polymer synthesis have allowed remarkable control over chain microstructure and conformation. Capitalizing on such developments, here we create well-controlled chain folding in sulfonated polyethylene, leading to highly uniform hydrated acid layers of subnanometre thickness with high proton conductivity. The linear polyethylene contains sulfonic acid groups pendant to precisely every twenty-first carbon atom that induce tight chain folds to form the hydrated layers, while the methylene segments crystallize. The proton conductivity is on par with Nafion 117, the benchmark for fuel cell membranes. We demonstrate that well-controlled hairpin chain folding can be utilized for proton conductivity within a crystalline polymer structure, and we project that this structure could be adapted for ion transport. This layered polyethylene-based structure is an innovative and versatile design paradigm for functional polymer membranes, opening doors to efficient and selective transport of other ions and small molecules on appropriate selection of functional groups.

Controlling molecular conformations to obtain desirable morphologies and properties is of both fundamental and technological importance[1,2]. Recent advances in polymer synthesis allow unprecedented control over chain microstructure, including the ability to place functional groups at precisely periodic intervals along a linear backbone[3-8]. Some of these precise polymers exhibit layered morphologies consisting of hairpin chain folds at the position of each functional group[9-11]. The degree of chemical and conformational control in these layered structures is a significant achievement, but associated useful properties have not been demonstrated until now.

Proton exchange membrane fuel cells depend on membranes such as Nafion to transport protons between electrodes while providing a mechanical and electronic barrier. Nafion has a complex multiscale phase-separated morphology with well-connected hydrophilic domains in which sulfonate-lined water channels percolate through a hydrophobic, semicrystalline polytetrafluoroethylene like matrix[12,13]. While the exact structure remains controversial[14-18], the water channels are thought to be nominally cylindrical[19,20]. For decades, researchers have sought to develop new membranes with lower production cost, higher operating temperature, lower operating humidity and other desirable attributes, using percolating hydrated domains as a design rule[21-27]. Most of these new polymers have amorphous, poorly controlled morphologies like Nafion, and are typically not on par with Nafion's performance. In striking contrast, controlled hairpin polymer folding is a cutting-edge, versatile strategy featuring a highly ordered morphology that holds promise for the development of new membranes to efficiently transport protons, ions and even small molecules.

There are a few examples of ion conductivity in polymers with crystal-like ordering. A hydrated polymer brush with ammonium terminated side chains formed a layered structure with periodicity of ~40 Å, with anionic (OH^-) conductivity of ~0.05 $S.cm^{-1}$, but the ordering was only moderate and the water channel structure was not quantified[28]. In membranes for batteries, it was shown that lithium ions can be transported along helical crystalline polyethylene oxide chains[29]. Ions can also be transported along the surfaces of polyethylene oxide crystallites[30].

Our innovative approach controls polymer folding to achieve a desirable, well-ordered, highly crystalline morphology with high proton conductivity. The success of this approach provides striking new insight into the design of proton- or other-ion-conducting synthetic membranes. Control of chain folding and morphology ismade possible by precise control of the chain microstructure via acyclic diene metathesis synthesis[5,8,31-34]. Our previous work showed that periodic placement of pendant atactic carboxyl groups along linear polyethylene produces controlled chain folding and layers of acid groups[9]. Here, sulfonic acid groups[35], which are highly hygroscopic moieties, replace carboxyl groups, producing hydrated layers with high proton conductivity. Our simulations show that the ordered, layered structure enhances diffusion relative to the tortuous water channels of an amorphous polymer. The layered polyethylene-based structure is a new design paradigm for functional polymer membranes, opening doors to efficient and selective transport of protons, ions and small molecules on appropriate chemistry selection.

Proton conductivity

The proton conductivity of a precisely sulfonated polyethylene, p21SA, as well as Nafion 117 for comparison, is plotted in Fig. 1a versus relative humidity (RH). The conductivities are obtained from EIS (Fig. 1d,e). The conductivities are very similar for 60% RH or greater-within a factor of 1.25. Such proton conductivity within

a polyethylene-based crystalline structure is new. At low RH, the conductivity of p21SA is appreciably lower than Nafion 117, due to the lower acidity of the alkyl sulfonic acid in p21SA compared with the fluoroalkyl sulfonic acid in Nafion.

The hydration number, λ, defined as the number of water molecules (including hydronium) per sulfonic group, is comparable in p21SA and Nafion 117 at low humidities, while Nafion has higher λ at high humidities (Fig. 1c). By volume, the water uptake is quite similar in p21SA and Nafion at high humidites (see Supplementary Fig. 1 for details).

The high conductivity of Nafion is attributed in part to the well-connected (percolated) hydrophilic domains achieved on hydration and the favourable nanoscale morphology with strong microphase separation[12,36]. As percolation of conductive domains is generally thought to be required for high conductivity, this suggests that the water/sulfonic acid domains are also percolated in p21SA. To assess the nature of the water domains in p21SA, X-ray scattering was performed as a function of RH.

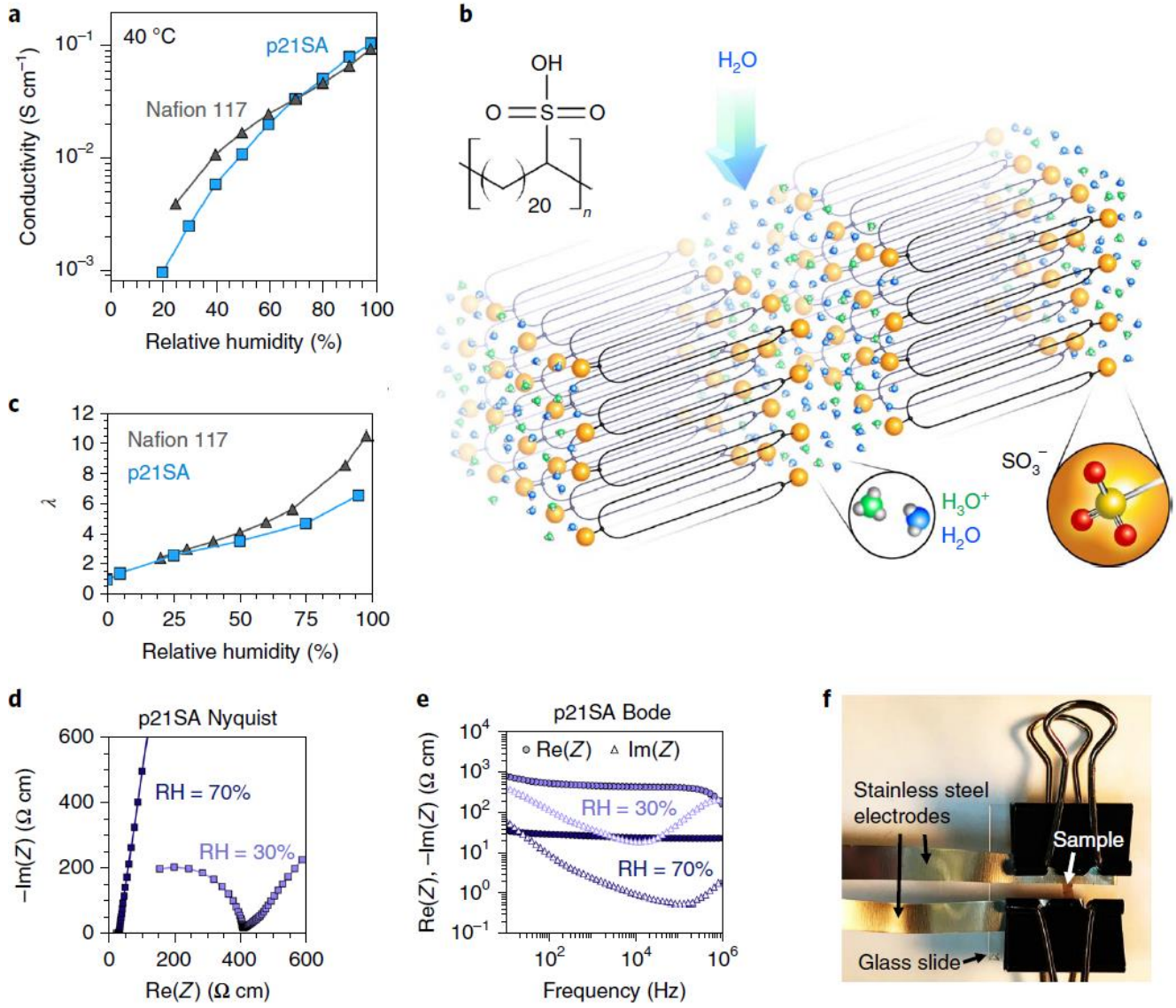

Fig. 1: Conductivity and water uptake of p21SA. **a**, DC conductivity of p21SA and Nafion 117 via EIS as a function of RH at 40°C. **b**, Chemical structure and schematic rendering of the secondary structure of hydrated p21SA, showing the crystalline backbones and acid-lined water layers. At bottom right, the yellow atom is sulfur and the red atoms are oxygen. **c**, Water uptake, λ, of p21SA and Nafion 117 (refs[47,48]) as a function of RH at 40°C. λ is defined as the number of water molecules per sulfonic group and is measured with a sorption balance. **d,e**, EIS Nyquist (d) and Bode (e) plots of the specific complex impedance (Z) of p21SA at 30% and 70% RH. For low humidities, part or all of the semicircle was evident in the EIS Nyquist plot, while at higher humidities, the proton conductivity timescale was faster than the maximum frequency of our impedance spectrometer (1 MHz). At all humidities, a minimum in -Im(Z) was evident in the Bode plot. The DC resistance was obtained from the value of Re(Z) at the frequency of minimum -Im(Z). **f**, Photo of p21SA sample connected to stainless steel electrodes for EIS measurements. The electrodes were connected laterally across the film, rather than in a sandwich-like manner, to maximally expose the sample to the air for improved equilibration on changing humidity.

Structural characterization

Recently, we elucidated the semicrystalline structure of a related polyethylene, with carboxyl groups pendant to every twenty first carbon atom (p21AA). We found that, within the crystalline domains, the backbones execute hairpin folds near the position of each acid group[9,10]. X-ray scattering of p21SA under vacuum is similar to

p21AA, showing a layered structure with scattering vector q = 0.22 $Å^{-1}$ (period = 28 Å) and a Bragg reflection at q = 1.5 $Å^{-1}$(d-spacing = 4.2 Å) (Fig. 2a). (Supplementary Fig. 3 contains additional X-ray scattering results.) This suggests that p21SA also exhibits the chain-folded structure, as depicted in Fig. 1b. The sulfonic acid groups form layers, with the crystalline alkyl segments between each layer. The two-dimensional (2D) X-ray scattering pattern (not shown here) is isotropic, indicating random orientation of crystalline domains. Alignment of the layers should further improve conductivity.

The X-ray scattering peak at 0.22 $Å^{-1}$ shifts to progressively lower q values as the RH is increased, corresponding to an increase in the layer period from 28 Å (1% RH) to 33 Å (65% RH). This indicates an expansion of the layered structure, depicted in Fig. 2c,d. When the water activity is increased, water enters the layers because of the hygroscopic sulfonic groups and the hydrophobic nature of the methylene groups. This expansion further supports our chain-folded model; if the chains were extended, the periodicity could not increase beyond the all-trans length of the repeating unit, 26.7 Å. Importantly, this swelling is reversible; the layer period decreases when the humidity is subsequently reduced.

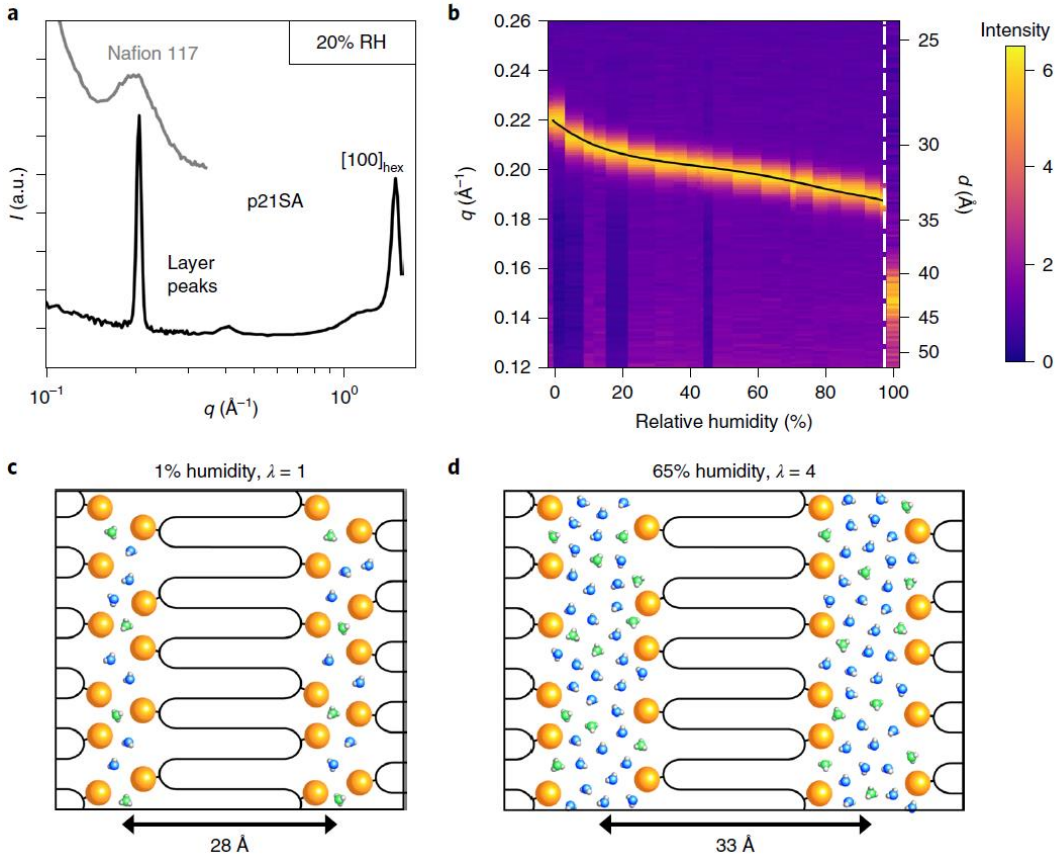

Fig. 2: X-ray scattering characterization of p21SA. **a**, Intermediate- and wide-angle X-ray scattering of p21SA at 20% RH at room temperature (21°C). Intermediate-angle X-ray scattering of Nafion 117 is shown for comparison. Scattering intensity I is plotted versus q. **b**, Primary layer peak of p21SA as a function of RH at 40°C, and immersed in water (far right). Each vertical strip is an I versus q curve. On the right y axis, q is converted to distance d using d = 2π/q. **c,d**, Schematic representation of the layered structure and the expansion of the layers on increasing environmental humidity. The structure contains many layers-at least 20, based on the Scherrer equation. The 100_{hex} peak in a, corresponding to alkyl segment packing, remains at constant position on changing λ (see Supplementary Table 1).

The uniformity of these layers is remarkably high. The primary layer peak has a full width at half maximum of ~0.01 $Å^{-1}$, equivalent to our instrumental resolution. Using the equation $\Delta q \approx 4\varepsilon q$, we obtain an upper limit to the dispersity, ε, of the layer period in the material, which is 0.4 Å or 1.2%. This small dispersity implies that virtually all sulfonic layers are accessible to surrounding water; there are essentially no sulfonic layers that are isolated from diffusing water. At 50% RH, there is no residual scattering intensity at the peak position of 1% humidity (see Fig. 2b), showing that essentially all layers have taken up water and expanded.

The crystal size and degree of crystallinity are key parameters in this system. While charge carrier mobility may be fast within the layers, grain boundaries may serve as impediments to mobility. In typical semicrystalline polymers (including polyethylene), small-angle X-ray scattering exhibits a long-period peak corresponding to intercrystallite distances; however, no such peak is present for p21SA within our instrumental range of q > 0.008 $Å^{-1}$ (d < 800 Å; see Supplementary Fig. 5). In contrast, the analogous carboxyl-containing polyethylene (p21AA) does exhibit a long period peak[8,9]. Applying the Scherrer equation to the primary sulfonic layer peak yields a minimum crystal size of ~700 Å along the vector normal to the layers. The peak breadth is equivalent to our instrumental resolution, so the size could be much larger. These two facts suggest an unusually large crystal size for p21SA. In fact, the morphology could resemble that of a long-spaced aliphatic polyester periodically

grafted with polytetrafluoroethylene side chains[11]. For this folded polyester, transmission electron microscopy revealed a layered morphology (period ~50 Å) persisting for hundreds of nanometres without noticeable amorphous regions. The Supplementary Information contains a detailed discussion of the crystallinity of p21SA. Future work will investigate grain size via transmission electron microscopy and the effect of grain size on conductivity.

Structure from simulations

Fully atomistic molecular dynamics (MD) simulations were carried out to further investigate the layered structure of p21SA. The starting structures of the simulations contained chain-folded molecules of atactic p21SA arranged in layers, similar to our previous work on p21AA[9]. A 2D slice of the relaxed structure is shown in Fig. 3a.

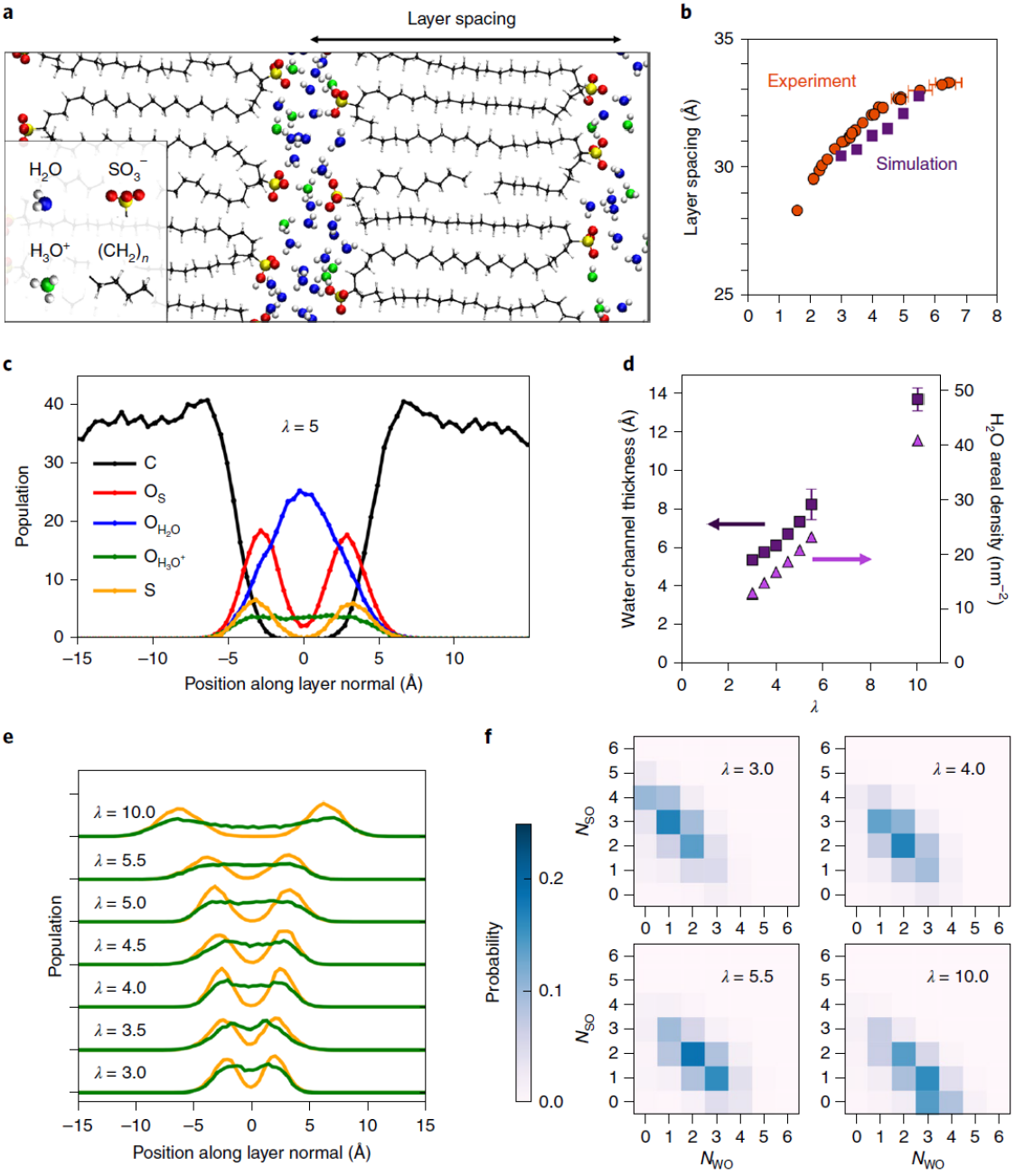

Fig. 3: Simulation results for the p21SA hydrated layered structure. **a**, Two-dimensional slice of a simulation snapshot showing the chain folding and hydrated acid layers. All atoms are shown in the CPK representation. **b**, Interlayer distance as a function of hydration number for experiments and simulations. The experimental layer spacing values are obtained from X-ray scattering. **c**, Projection of atomic positions onto the vector normal to the acid layers, averaged over 10 ns (200 frames). The carbon population has a slight maximum approximately 6 Å from the layer centre due to the chain folds. **d**, From simulations, water layer thickness as a function of hydration number, obtained from the full width at half maximum of the sum of the OH_2O and OH_2O^+ profiles in c (squares). The nonlinearity at low λ is due to sulfonate groups occupying some of the water layer volume. The areal density of water molecules (H_2O and H_3O^+) within each acid layer (triangles) are also shown. **e**, Position of hydronium and sulfur as in c, for seven hydration levels. **f**, Probability heat map of the coordination number (N) of hydronium oxygens coordinated to sulfur (SO, y axis) and of the same hydronium oxygens coordinated to water oxygen (WO, x axis)[49]. With increasing λ, this shows the transition from hydroniums being primarily bound to sulfonate groups to being primarily bound to water.

The interlayer distance obtained from simulations is compared with experiments as a function of hydration number λ in Fig. 3b. We find good agreement between simulations and experiments, to within 1 Å (3%). This suggests that our simulated structures are close to experiments and verifies the chain-folded model proposed in Fig. 1b. For $3 \leq \lambda \leq 5.5$, the slope is approximately 0.8 Å per unit λ, agreeing well with experiment. The chain-folded structure is consistent with the reversibility of the swelling. We only simulate systems with $\lambda \geq 3$, where the sulfonic acid groups are fully ionized.

In Fig. 3c, atoms from the $\lambda = 5$ simulation are projected onto the vector normal to the layer plane to display the average composition of the layer. Aside from carbon, the sulfur is farthest from the layer centre, followed by sulfonate oxygen, showing that the sulfonate groups tend to be oriented with their dipoles towards the layer centre. Most of the water molecules are near the layer centre, along with some penetration near the layer walls. In contrast, the H_3O^+ are distributed quite evenly at $\lambda = 5$ between the layer centre and the average sulfur position towards the sides of the layer.

Intriguing advantages of this unusual hairpin structure include (1) highly percolating water domains that reduce barriers to water and charge carrier mobility, (2) well-controlled, tunable water environments, allowing detailed study and optimization of environments that produce high charge carrier mobility, (3) well-defined, tunable melting point, which is defined by the alkyl spacer length, (4) mechanical integrity provided by crystalline alkyl segments and (5) strong phase separation of water from the alkyl phase due to crystalline packing of alkyl segments.

The position distributions of the hydroniums are shown as a function of λ in Fig. 3e. The small peaks near the sulfonate groups indicate a slight preference for the layer walls due to electrostatic interactions, but many hydroniums are also near the channel centre, solvated by water. This suggests heterogeneous hydronium dynamics-those hydroniums close to sulfonic groups experience reduced mobility due to electrostatics, while those towards the centre of the layer are solvated by the water and thus more mobile. As λ increases, the distribution broadens, and hydronium is increasingly likely to be solvated by water. This is also apparent in Fig. 3f, where for $\lambda = 3$, a hydronium is likely to be coordinated to zero or one water molecule, while when $\lambda = 5.5$, the most likely hydronium coordination states are (1) two sulfonates and two waters or (2) one sulfonate and three waters.

Water dynamics from simulations

Using simulations, we quantify the water molecule dynamics within the hydrated layers in p21SA. Although our hydronium approximation does not treat (directly) proton quantum dynamics, for example, Grotthuss diffusion[37-39], we obtain insights into the dynamics with this approach. In proton exchange membranes, the proton conductivity is generally related to the local viscosity and the tortuosity of the conductive domains[38], and the water diffusion coefficient, D_{H2O}, captures these parameters. The primary simulations treat the water dynamics in a crystalline structure (that is, single grain). These dynamics do not depend crucially on quantum transport, and thus the simulation data should correspond well to that in the measurements[40]. We also quantify the water dipole rotation rate, τ^{-1}_{H20}, via the orientation autocorrelation; τ^{-1}_{H20} can be considered a measure of the local viscosity within the hydrated domains.

D_{H2O} and τ^{-1}_{H20} in crystalline p21SA are plotted in Fig. 4d,e, respectively. Both quantities exhibit an exponential decay versus λ^{-1}. In aqueous acid solutions, a similar exponential decay of water dynamics is experimentally observed as a function of acid concentration. Meanwhile, simulations of water confined in one dimension (that is, thin layer) with neutral pH and hydrophobic surfaces showed a roughly linear dependence of water diffusion on degree of confinement [41,42]. In p21SA, the water dynamics are inhibited by both the high ion concentration and the high degree of confinement. For our most confined simulation, where $\lambda = 3$ (in Fig. 3d, areal water density of 12 nm^2), D_{H2O} is reduced by a factor of ~60, while D_{H2O} under non-ionic confinement at the same areal density was reduced by a factor of ~10 (ref.[41]).

To further characterize the water dynamics in the crystalline (layered) p21SA structure shown in Fig. 4b, comparisons are made with several other systems: bulk water, methanesulfonic acid ($MeSO_3H$) solutions (0.2–14 M concentrations; Fig. 4a) and amorphous p21SA (Fig. 4c). Bulk water should provide the low-λ^{-1} limit, and both D_{H2O} and τ^{-1}_{H20} for crystalline p21SA extrapolate nearly perfectly to bulk water values. The $MeSO_3H$ data reveals the effect of the acidic interactions in bulk. For $MeSO_3H$, at very low λ^{-1}, D_{H2O} and τ^{-1}_{H20} decrease from bulk water with similar exponential dependence to crystalline p21SA, while at higher λ^{-1} the dynamics plateau to values related to the viscosity of neat $MeSO_3H$. The impact of the layered geometry is demonstrated by comparing results from simulations based on the experimentally observed crystal structure with those of an amorphous structure with disordered water channels. While τ^{-1}_{H20} in the amorphous p21SA simulations is similar to that of the crystalline simulation, even exceeding it by a factor of 1.2, D_{H2O} is substantially lower in the amorphous simulation, by a factor of 2 to 3.

The water rotational dynamics appears to be the controlling factor for diffusion in crystalline p21SA, as evidenced by plotting D_{H2O} versus τ^{-1}_{H20} (Fig. 4f). As expected, in the $MeSO_3H$ solutions, diffusion is directly controlled by the water rotation rate, clearly falls on the same line as $MeSO_3H$ and bulk water when the 2D diffusion coefficient ($D = MSD / 4t$, where MSD is mean square displacement and t is time) is considered (stars).

Thus, the water diffusion in crystalline p21SA is controlled by water rotation rate to the same extent as the $MeSO_3H$, after accounting for the dimensionality of diffusion.

In contrast, the 3D water diffusion coefficient in amorphous p21SA falls significantly below the line in Fig. 4f, by a factor of 4 to 5. While the dimensionality of the amorphous system is difficult to determine, even the 1D diffusion coefficient (D = MSD / 2t) would be below the line. We attribute this to the nonuniformity of the water domains in amorphous p21SA. As depicted in Fig. 4c, amorphous p21SA contains large water domains connected by narrow water channels. Thus, the average rotation rate is likely dominated by the water in the large domains, while the diffusion is limited by the transport of water through the narrow channels. This amorphous morphology therefore hinders water diffusion, while the crystalline structure does not. This is also seen in Fig. 4i: water in the amorphous simulations remains subdiffusive[43] until it travels the length of the simulation box (58 Å), compared with Fig. 4g,h, where the water is diffusive at t < 1 ns. A larger simulation box may result in even more reduced D_{H2O} in amorphous p21SA. Therefore, ordered water layers are desirable in fuel cell membranes relative to disordered water channels; according to our simulations, they lead to more efficient water diffusion (and therefore proton conductivity) given the same chemistry and hydration level.

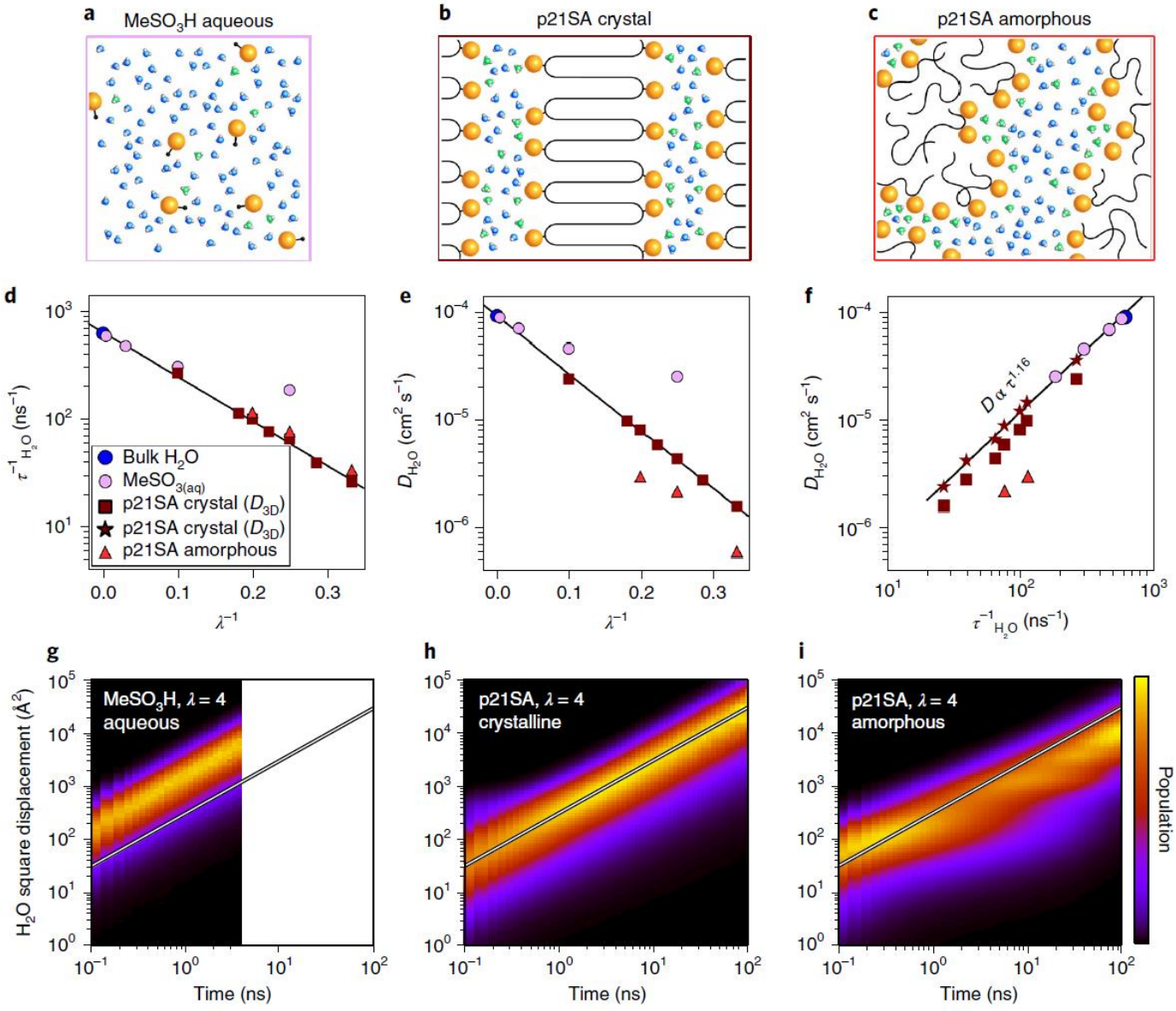

Fig. 4: Water dynamics from simulations of bulk water, $MeSO_3H$ solution, crystalline p21SA and amorphous p21SA. **a-c**, Schematics of $MeSO_3H$ solution (a), crystalline p21SA (b) and amorphous p21SA (c). **d**, Water molecular dipole rotation rate as a function of inverse hydration number, λ^{-1}. **e**, Diffusion coefficient of water as a function of inverse hydration number. **f**, Diffusion coefficient of water as a function of dipole rotation rate. **g-i**, Distribution of squared displacements of water molecules versus time-delta for $MeSO_3H$ (g), crystalline p21SA (h) and amorphous p21SA (i) simulations. The lines have slopes of 1 on this log-log plot, and all have the same y intercept. The crystalline p21SA and aqueous $MeSO_3H$ simulations are uniformly diffusive for time > 0.1 ns, while the amorphous simulation is not diffusive even when the water has moved close to the simulation box size (58 Å or 3,400 $Å^2$). All plotted diffusion coefficients are 3D except stars in f, which are 2D. In g, the simulation of aqueous $MeSO_3H$ was only carried out to 40 ns.

Conclusion and outlook

We have demonstrated that controlled polyethylene folding can produce desired transport properties, and that a crystalline structure can promote proton transport in a polymer. Simply by placing sulfonic acid groups on precisely every twenty-first carbon, linear polyethylene executes hairpin chain folds at the position of each sulfonic acid group, triggering a directed self-assembly into a crystalline structure containing water layers of subnanometre thickness. The resulting structure has proton conductivity on par with Nafion 117, despite the lower acidity of alkylsulfonic acid functional moieties in p21SA. We have demonstrated the use of controlled polyethylene folding to produce desired transport properties, as well as an example of a crystalline structure promoting proton transport in a polymer. The conductivity could be further improved by aligning the layers (for example, by mechanical shearing, AC/DC electric or magnetic field, directional epitaxial solidification or directed self-assembly techniques) such that the layer normal is orthogonal to the desired transport direction. This alignment would also provide anisotropic conductivity. Furthermore, our simulations suggest that the high degree of ordering of the water domains in p21SA improves proton conductivity relative to random, tortuous water channels. The effect of ordered layers, as well as the role of grain boundaries, on water diffusion will be further investigated via NMR relaxometry in comparison with Nafion and other sulfonic acid-based proton conducting polymers[44]. Our strategy of using polyethylene crystallization to achieve high proton conductivity is a cutting-edge alternative paradigm with respect to other strategies in the literature, most of which use polymers containing sulfonated aromatic rings that have highly disordered to poorly ordered morphologies.

This work has broad implications beyond hydrated fuel cell membranes, as various functional groups could be incorporated without disrupting the highly advantageous layers. This robust and versatile layered structure could be engineered and modified for applications in anhydrous fuel cell membranes, cation or anion conductive membranes for batteries, and water purification membranes. It remains to be explored whether a small molecule (in this study, water) is required for efficient transport. Perhaps replacing the sulfonic acid group with an ionic liquid functionality-protic, such as imidazole[45], or aprotic-could allow anhydrous proton transport or cation/anion transport, respectively, through the layers, leading to next-generation electrochemical energy storage solutions. Similarly, the concentrated acid groups within the layers may provide high cation (for example, Li^+, Na^+, K^+) conductivity even in the absence of water, because the proximity of the acid groups could allow efficient ion transport. Future work should examine the mechanical properties of these precisely sulfonated polyethylene films, as mechanical performance is critical for use in fuel cells and other applications. Routes to improving the mechanical properties could be (1) improving the crystal integrity by increasing the alkyl length between sulfonic groups and/or incorporating H-bonding groups (for example, amides) into the backbone, and (2) inducing the formation of amorphous domains to increase elasticity, for example, by terminating chains with non-crystallizable groups. Future work will also examine whether this structure and corresponding conductivity is present in nearly precise polymers, wherein the functional group placement is variable by one carbon[46].

Methods

Methods, including statements of data availability and any associated accession codes and references, are available at https://doi.org/10.1038/s41563-018-0097-2 .

Materials. The synthesis of p21SA was carried out via acyclic diene metathesis polymerization, as reported previously[35,50,51]. This linear, atactic polyethylene contains one sulfonic acid group pendant to precisely every twenty-first carbon atom along the chain. Size exclusion chromatography characterization of p21SA gives a number-average molecular weight (M_n) of 19.8 kg.mol^{-1}, and a dispersity index ($D_w = M_w/M_n$) of 2.4. Note that p21SA is readily soluble in DMSO.

Differential scanning calorimetry with cooling and heating scans using a rate of 10°C.min^{-1} indicated a melting temperature (Tm) of 65 °C when dry, see Supplementary Fig. 6. Nafion 117 was obtained from Sigma-Aldrich (ref. 274674).

X-ray scattering. X-ray scattering data were collected using the Multi-Angle X-ray Scattering (MAXS) Facility at the University of Pennsylvania. The X-ray wavelength was 1.542 Å and a variety of sample-detector distances were used (54, 11 and 7 cm). For X-ray scattering with controlled humidity, an environmental chamber was used, which controls the ratio of dry and humid air flowing into the chamber, as well as the temperature of the incoming air and of the chamber itself[52]. The chamber is equipped with a temperature and humidity sensor located approximately 2 cm from the sample. Primary analysis of X-ray data was performed using the Datasqueeze software (version 3.0.7)[53].

p21SA samples were prepared for X-ray scattering by hot pressing at 80 °C for 10 min (thickness of ca. 50 μm), then performing the following thermal treatment: the sample was melted in a humidity-controlled chamber at 90°C and 50% RH for at least 2 h, followed by cooling at 1 °C.min^{-1} to 25°C with RH maintained at 50%. All humidity-controlled X-ray scattering experiments were performed at 40°C. Stabilization of the X-ray scattering at a given condition was confirmed by the following method: the X-ray scattering pattern was monitored by performing 5 min scans continuously until the pattern stabilized (1 to 3 h).

EIS. EIS was performed using a Solartron ModuLab XM MTS with the femtoammeter accessory. The controlled sample environment was provided by a Thermotron environmental chamber (SM-1.0-3200). Terminals from the ModuLab instrument were fed through the chamber wall to access the sample. p21SA was hot-pressed to a thickness of 200 μm and cut into a rectangular strip. After performing the same thermal treatment as was done

for X-ray scattering samples, this strip was placed on a glass slide, and ribbons of stainless-steel foil (thickness of 130 μm) were secured to both sides of the sample using binder clips, and were connected to the EIS as electrodes. For additional details, see Fig. 1f. The cell constant was measured by (1) measuring the thickness of the sample with a micrometer before application of the stainless-steel electrodes, and (2) taking a photo of the sample with the electrodes attached and measuring the length and width using the ImageJ software[54]. Sample dimensions were a length of 8 mm, a width of 3 mm and a thickness of 200 μ m. The sample was held at desired RH and EIS was measured repeatedly until stable (several hours). DC proton conductivity was obtained from the value of Re(Z) at the minimum of Im(Z) on a Bode plot.

Atomistic MD simulations. Fully atomistic MD simulations were carried out using the LAMMPS software package[55]. Alkyl segments were modelled using the LOPLS force field[56] as in our previous work[9,57], sulfonate groups used the parameters developed in ref.[58], water molecules used the TIP3P parameters[59], and hydronium molecules used parameters developed in ref.[60]. Periodic boundary conditions were used in all simulations. The real-space nonbonded cutoff was 13 Å and a particle-particle particle-mesh solver was used for long-range electrostatics[61]. A Nosé-Hoover thermostat was used with a temperature damping parameter of 102 fs and a pressure damping parameter of 105 fs. The integration time step was 1 fs.

Crystalline p21SA initial structures were constructed identically to our previous publication on precise carboxylic acid polyethylene (p21AA)[9], except we replaced the carboxylic acid with sulfonate, and water and hydronium molecules were placed between the layers of sulfonate groups. Each p21SA molecule was made atactic using a random number generator and consisted of four monomeric units (84 carbon atoms). The sulfonic groups were assumed to be 100% ionized, so $[H_3O^+] = [SO_3^-]$ and $[SO_3H] = 0$; see Supplementary Fig. 4 for infrared absorption spectroscopy evidence of this. Water molecules were initially placed between the layers of p21SA molecules, including the correct number of H_3O^+ molecules to balance the charge of the SO_3^- groups in each layer. Each layer contained the same number of water and hydronium molecules, where this number corresponded to the hydration number λ of the simulation. λ is the number of water molecules (including hydronium) per sulfonic acid group.

All crystalline p21SA simulations used the following procedure for MD simulations. First, a local energy minimization was carried out with stopping tolerance of 10^4 (ratio) for energy and 10^4 kcal.mol.Å^{-1} for force. Then the Nosé-Hoover thermostat was turned on and run at 273 K for 1 ns with the NPT ensemble and the 'triclinic' option, for initial low-temperature relaxation. Then the system was heated to 348 K at a rate of 10 K ns^{-1}, and structural relaxation proceeded at 348 K for at least 65 ns or until the H_2O molecules reached the diffusive regime.

For the amorphous p21SA simulations, initial structures contained all-trans p21SA molecules, H_2O molecules, and H_3O^+ molecules at a density of ca. 0.004 g.cm^{-3} with large spacing between each molecule, similar to previous studies[62-64]. The system was isotropically compressed to a density of ~0.06 g.cm^{-3} at 423 K using a Langevin thermostat. Then the Nosé-Hoover thermostat was used to equilibrate the system in the NPT ensemble at 423 K for at least 70 ns, followed by cooling to 348 K at 10 K.min^{-1}. Then the system was run at 348 K for at least 100 ns in the NPT ensemble.

For the aqueous $MeSO_3H$ simulations and pure H2O simulations, initial structures had densities less than 0.01 g.cm^{-3}. The systems were isotropically compressed to moderate density at 348 K using a Langevin thermostat, then were equilibrated at 348 K for at least 2 ns using the Nosé-Hoover thermostat with NPT ensemble before commencing dynamics measurements.

Coordination states of hydronium molecules (Fig. 3f) were obtained in the following manner. For each hydronium, all water molecules at a distance falling within the first peak of a $g(r)_{H3O-H2O}$ plot were counted, where $g(r)_{x-y}$ is the partial radial distribution function involving species x and y. Similarly, all sulfonic groups at a distance corresponding to the first peak of a $g(r)_{H3O-SO3}$ plot were counted. This was done for all hydronium molecules in the system and averaged over 25 frames (12.5 ns).

Rotation times of H_2O were obtained from simulations by fitting the molecular dipole autocorrelation function with a stretched exponential function. The fit was limited to t > 30 fs to avoid librational motions. See Supplementary Fig. 8 for details. Diffusion coefficients of H_2O and H_3O^+ were obtained by plotting the derivative of the MSD with respect to time and extracting the value of the derivative after it became time-independent at long times. MSD plots of water molecules in the crystalline simulations are available in Supplementary Fig. 9.

Water sorption. For the gravimetric water sorption experiments, we used a SGA- 100 Symmetrical Gravimetric Analyzer from VTI Corporation with a Dew point monitor (Edgetech-Dew Prime I) and a Cahn D-200 digital recording balance. The sample (thickness of 150 μ m) was loaded into the balance and dried at 60°C under dry air for 10 h. Then, the chamber was set to 0% humidity and 40 °C and the sample was equilibrated for 3 h. The humidity was stepped up to each measured value and the equilibration time was 3 h for each step. Then the humidity was stepped down similarly, and we used an average of the masses measured on increasing and decreasing humidity. Because 60°C is not sufficient to completely dry the sample, we supplemented these experiments with thermogravimetric analysis (TGA). The sample was equilibrated to room conditions (22 °C and 56% RH), the mass was measured, and then it was placed in the TGA and heated to 110 °C for 10 h. The mass change was assumed to be the total water content of the sample at the room conditions. The data from the sorption balance were then modified accordingly.

Synchrotron-source infrared absorbance. Mid-infrared absorbance spectra were measured at the AILES beamline65 at the SOLEIL facility[66] with a Bruker IFS125 FTIR spectrometer using synchrotron mid-infrared radiation. Spectra were obtained by averaging 200 scans. Spectra were recorded using a KBr beam splitter and a MCT detector with a resolution of 4 cm^{-1} at 2 $cm.s^{-1}$ mirror speed. All measurements were mainly done at 25°C. A specific homemade cell[67] was used to measure hydration/dehydration in situ processes. The membrane (6 mm by 6 mm by 150 µm) was placed inside the cell, perpendicularly to the incident beam exposed to the humidified air/pumping allowing the hydration/dehydration processes. As described elsewhere[68], sample temperature is controlled by a cryostat (precision 0.05 K), while sample hydration is monitored by a thermostated gauge (0-100 mbar with a precision of 0.02 mbar). The gauge provides control of the water vapour pressure (p) in the cell. The RH to which the membrane is exposed can be precisely set to the value (p/p_0) × 100, p_0 being the water vapour pressure equal to 28 mbar at 23 °C.
The p21SA membrane was first dried in situ and the water vapour pressure was set to ca. 2×10^5 mbar. For hydration, increasing vapour pressures were successively applied until the final hydration at 92% vapour pressure. All spectra are displayed in absorbance units as $-\log(I/I_0)$, where I and Io are the sample and empty cell transmissions, respectively.

Acknowledgements
E.B.T and K.I.W. acknowledge funding from the National Science Foundation (NSF) DMR 1506726, NSF PIRE 1545884, and the Army Research Office W911NF1310363. T.W.G. and K.B.W. thank the National Science Foundation (DMR1505778) for partial financial support for this project. This material also is based on catalyst work supported by, or in part by, the Army Research Office under the grant W911NF1310362. E.B.T, M.M. and P.R. acknowledge support from the Centre national de la recherche scientifique (CNRS) at the laboratoire des Systèmes Moléculaires et nanoMatériaux pour l'Energie et la Santé in Grenoble, France (UMR5819-SyMMES (CNRS/CEA/Univ. Grenoble Alpes)), and funding from the Agence Nationale de le Recherche (ANR): ANR-15-PIRE-0001-01 and ANR-15-PIRE-0001-07. D.E.M. acknowledges funding from Rachleff Scholars Program of the University of Pennsylvania. This work was performed, in part, at the Center for Integrated Nanotechnologies, an Office of Science User Facility operated for the US Department of Energy (DOE) Office of Science. Sandia National Laboratories is a multimission laboratory managed and operated by National Technology and Engineering Solutions of Sandia, LLC, a wholly owned subsidiary of Honeywell International, Inc., for the US Department of Energy's National Nuclear Security Administration under contract DE-NA-0003525. We acknowledge the Laboratory for Research on the Structure of Matter (LRSM), supported by NSF DMR 11-20901. We acknowledge support from the Army Research Office Defense University Research Instrumentation Program (ARO DURIP) grant W911NF-14-1-0466. We acknowledge the Synchrotron SOLEIL for beamtime and financial support, and J.-B. Brubach as a local contact on the AILES beamline for the infrared absorbance data at various humidities. We acknowledge H. Mendil-Jakani for assistance with preliminary X-ray scattering measurements and E. Dubard for experimental support. This research used resources of the Advanced Photon Source, a US DOE Office of Science User Facility operated for the DOE Office of Science by Argonne National Laboratory under contract no. DE-AC02-06CH11357. In particular we acknowledge E. Bailey and S. Narayanan of beamline 8-ID-I for the small-angle X-ray scattering data presented in Supplementary Fig. 5. We thank A. Frischknecht (Sandia National Laboratories), A. Patel (University of Pennsylvania) and L. Gonon (UMR5819-SyMMES (CNRS/CEA/Univ. Grenoble Alpes)) for helpful discussions. We thank Materia Inc. for their generous donation of the catalyst used in this project. We thank C. Lee Georgescu for illustrating Figs. 1b, 2c,d and 4a-c.

Author contributions
E.B.T. and K.I.W. generated the main ideas of the project, measured X-ray scattering, conductivity and sorption, performed simulations, analysed all data and wrote most of the text of this paper. T.W.G. and K.B.W. conceived of and carried out the synthesis of the polymer. M.M. and P.R. contributed ideas and interpretation and edited the text. M.M. collected infrared absorbance data and sorption data. D.E.M. collected conductivity data. M.J.S. contributed simulation expertise, ideas and interpretation, and edited the text.

Competing interests
The authors declare no competing interests.

Additional information
Supplementary information is available for this paper at https://doi.org/10.1038/s41563-018-0097-2 .
Reprints and permissions information is available at www.nature.com/reprints.
Correspondence and requests for materials should be addressed to K.I.W.
Publisher's note: Springer Nature remains neutral with regard to jurisdictional claims in published maps and institutional affiliations.
Nature

Data availability.
The data that support the plots are available from the corresponding author upon reasonable request.

References

1. Dobson, C. M. Protein folding and misfolding. *Am. Sci.* **90**, 445-453 (2002).
2. Hill, D. J., Mio, M. J., Prince, R. B., Hughes, T. S. & Moore, J. S. A field guide to foldamers. *Chem. Rev.* **101**, 3893-4011 (2001).
3. Ortmann, P. & Mecking, S. Long-spaced aliphatic polyesters. *Macromolecules* **46**, 7213-7218 (2013).
4. Le Fevere de Ten Hove, C., Penelle, J., Ivanov, D. A. & Jonas, A. M. Encoding crystal microstructure and chain folding in the chemical structure of synthetic polymers. *Nat. Mater.* **3**, 33-37 (2004).
5. Atallah, P., Wagener, K. B. & Schulz, M. D. ADMET: the future revealed. *Macromolecules* **46**, 4735-4741 (2013).
6. Gaines, T. W., Trigg, E. B., Winey, K. I. & Wagener, K. B. High melting precision sulfone polyethylenes synthesized by ADMET chemistry. *Macromol. Chem. Phys*. **217**, 2351-2359 (2016).
7. Caire da Silva, L., Rojas, G., Schulz, M. D. & Wagener, K. B. Acyclic diene metathesis polymerization: history, methods and applications. *Prog. Polym. Sci.* **69**, 79-107 (2017).
8. Baughman, T., Chan, C., Winey, K. & Wagener, K. B. Synthesis and morphology of well-defined poly(ethylene-*co*-acrylic acid) copolymers. *Macromolecules* **40**, 6564-6571 (2007).
9. Trigg, E. B., Stevens, M. J. & Winey, K. I. Chain folding produces a multilayered morphology in a precise polymer: simulations and experiments. *J. Am. Chem. Soc.* **139**, 3747-3755 (2017).
10. Trigg, E. B., Middleton, L. R., Moed, D. E. & Winey, K. I. Transverse orientation of acid layers in the crystallites of a precise polymer. *Macromolecules* **50**, 8988-8995 (2017).
11. Mandal, J., Krishna Prasad, S., Rao, D. S. S. & Ramakrishnan, S. Periodically clickable polyesters: study of intrachain self-segregation induced folding, crystallization, and mesophase formation. *J. Am. Chem. Soc.* **136**, 2538-2545 (2014).
12. Gierke, T. D., Munn, G. E. & Wilson, F. C. The morphology in nafion perfluorinated membrane products, as determined by wide- and small-angle X-ray studies. *J. Polym. Sci. Polym. Phys. Ed.* **19**, 1687-1704 (1981).
13. Eisenberg, A. Clustering of ions in organic polymers. A theoretical approach. *Macromolecules* **3**, 147-154 (1970).
14. Diat, O. & Gebel, G. Fuel cells: proton channels. *Nat. Mater.* **7**, 13-14 (2008).
15. Kreuer, K. D. & Portale, G. A critical revision of the nano-morphology of proton conducting ionomers and polyelectrolytes for fuel cell applications. *Adv. Funct. Mater.* **23**, 5390-5397 (2013).
16. Mauritz, K. A. & Moore, R. B. State of Understanding of Nafion. *Chem. Rev.* **104**, 4535-4585 (2004).
17. Kusoglu, A., Mosdestino, M. A., Hexemer, A., Segalman, R. A. & Weber, A. Z. Subsecond morphological changes in Nafion during water uptake detected by small-angle X-ray scattering. *ACS Macro Lett.* **1**, 33-36 (2012).
18. Kreuer, K. D. Ion conducting membranes for fuel cells and other electrochemical devices. *Chem. Mater*. **26**, 361-380 (2013).
19. Rubatat, L., Rollet, A. L., Gebel, G. & Diat, O. Evidence of elongatedpolymeric aggregates in Nafion. *Macromolecules* **35**, 4050–4055 (2002).
20. Schmidt-rohr, K. & Chen, Q. Parallel cylindrical water nanochannels in Nafion fuel-cell membranes. *Nat. Mater.* **7**, 75-83 (2008).
21. Li, N. & Guiver, M. D. Ion transport by nanochannels in ion-containing aromatic copolymers. *Macromolecules* **47**, 2175-2198 (2014).
22. Vetter, S., Ruffmann, B., Buder, I. & Nunes, S. P. Proton conductive membranes of sulfonated poly(ether ketone ketone). J. Memb. Sci. 260,181–186 (2005).
23. Fujimoto, C. H., Hickner, M. A., Cornelius, C. J. & Loy, D. A. Ionomeric poly(phenylene) prepared by Diels-Alder polymerization: synthesis and physical properties of a novel polyelectrolyte. *Macromolecules* **38**, 5010-5016 (2005).
24. Elabd, Y. A. & Hickner, M. A. Block copolymers for fuel cells. *Macromolecules* **44**, 1-11 (2011).
25. Elabd, Y. A., Napadensky, E., Walker, C. W. & Winey, K. I. Transport properties of sulfonated poly(styrene-*b*-isobutylene-*b*-styrene) triblock copolymers at high ion-exchange capacities. *Macromolecules* **39**, 399-407 (2006).
26. Kim, H. K., Zhang, M., Yuan, X., Lvov, S. N. & Chung, T. C. M. Synthesis of polyethylene-based proton exchange membranes containing PE backbone and sulfonated poly(arylene ether sulfone) side chains for fuel cell applications. *Macromolecules* **45**, 2460-2470 (2012).
27. Nakabayashi, K., Higashihara, T. & Ueda, M. Polymer electrolyte membranes based on cross-linked highly sulfonated multiblock copoly(ether sulfone)s. *Macromolecules* **43**, 5756-5761 (2010).
28. Miyanishi, S., Fukushima, T. & Yamaguchi, T. Synthesis and property of semicrystalline anion exchange membrane with well-defined ion channel structure. *Macromolecules* **48**, 2576-2584 (2015).
29. Gadjourova, Z., Andreev, Y. G., Tunstall, D. P. & Bruce, P. G. Ionic conductivity in crystalline polymer electrolytes. *Nature* **412**, 520-523 (2001).
30. Cheng, S., Smith, D. M. & Li, C. Y. How does nanoscale crystalline structure affect ion transport in solid polymer electrolytes? *Macromolecules* **47**, 3978-3986 (2014).

31. Schulz, M. D., Sauty, N. F. & Wagener, K. B. Morphology control in precision polyolefins. *Appl. Petrochem. Res.* **5**, 3-8 (2015).
32. Buitrago, C. F. *et al.* Room temperature morphologies of precise acid- and ion-containing polyethylenes. *Macromolecules* **46**, 9003-9012 (2013).
33. Middleton, L. R. *et al.* Hierarchical acrylic acid aggregate morphologies produce strain-hardening in precise polyethylene-based copolymers. *Macromolecules* **48**, 3713-3724 (2015).
34. Seitz, M. E. *et al.* Nanoscale morphology in precisely sequenced poly(ethylene-co-acrylic acid) zinc ionomers. *J. Am. Chem. Soc.* **132**, 8165-8174 (2010).
35. Gaines, T. W., Bell, M.H., Trigg, E. B., Winey, K. I. & Wagener, K. B. Precision sulfonic acid polyolefins via heterogenous to homogenous deprotection. *Macromol. Chem. Phys.* https://doi.org/10.1002/macp.201700634 (2018).
36. Kreuer, K. D., Paddison, S. J., Spohr, E. & Schuster, M. Transport in proton conductors for fuel cell applications: simulation, elementary reactions and phenomenology. *Chem. Rev.* **104**, 4637-4678 (2004).
37. Feng, S. & Voth, G. A. Proton solvation and transport in hydrated Nafion. *J. Phys. Chem. B* **115**, 5903-5912 (2011).
38. Choi, P., Jalani, N. H. & Datta, R. Thermodynamics and proton transport in Nafion. *J. Electrochem. Soc.* **152**, E123-E130 (2005).
39. Suarez, S. N., Jayakody, J. R. P., Greenbaum, S. G., Zawodzinski, T. & Fontanella, J. J. A fundamental study of the transport properties of aqueous superacid solutions. *J. Phys. Chem. B* **114**, 8941-8947 (2010).
40. Urata, S. et al. Molecular dynamics simulation of swollen membrane of perfluorinated ionomer. *J. Phys. Chem. B* **109**, 4269-4278 (2005).
41. Lane, J. M. D., Chandross, M., Stevens, M. J. & Grest, G. S. Water in nanoconfinement between hydrophilic self-assembled monolayers. *Langmuir* **24**, 5209-5212 (2008).
42. Leng, Y. & Cummings, P. T. Fluidity of hydration layers nanoconfined between mica surfaces. *Phys. Rev. Lett.* **94**, 19-22 (2005).
43. Savage, J. & Voth, G. A. Persistent subdiffusive proton transport in perfluorosulfonic acid membranes. *J. Phys. Chem. Lett.* **5**, 3037-3042 (2014).
44. Perrin, J., Lyonnard, S., Guillermo, A. & Levitz, P. Water dynamics in ionomer membranes by field-cycling NMR relaxometry. *J. Phys. Chem. B* **110**, 5439-5444 (2006).
45. Jankowska, A., Zalewska, A., Skalska, A., Ostrowski, A. & Kowalak, S. Proton conductivity of imidazole entrapped in microporous molecular sieves. *Chem. Commun*. **53**, 2475-2478 (2017).
46. Trigg, E. B., Tiegs, B. J., Coates, W. & Winey, K. I. High morphological order in a nearly precise acid-containing polymer and ionomer. *ACS Macro Lett.* **6**, 947-951 (2017).
47. Zawodzinski, T. A. *et al.* Water uptake by and transport through Nafion 117 membranes. *J. Electrochem. Soc.* **140**, 1041-1047 (1993).
48. Yin, Y. *et al.* Synthesis, proton conductivity and methanol permeability of a novel sulfonated polyimide from 3-(2′ ,4′ -diaminophenoxy)propane sulfonic acid. *Polymer* **44**, 4509-4518 (2003).
49. Abbott, L. J. & Frischknecht, A. L. Nanoscale structure and morphology of sulfonated polyphenylenes via atomistic simulations. *Macromolecules* **50**, 1184-1192 (2017).
50. Gaines, T. W. Oxidized Sulfur Functionalized Polymers via ADMET Polymerization. PhD thesis, Univ. Florida (2015).
51. Gaines, T. W. & Wagener, K. B. Sulfonated polyethylene. US patent 9,724,686 (2017).
52. Salas-De La Cruz, D. *et al.* Environmental chamber for in situ dynamic control of temperature and relative humidity during X-ray scattering. *Rev. Sci. Instrum.* **83**, 025112 (2012).
53. Heiney, P. Datasqueeze: a software tool for powder and small-angle X-ray diffraction analysis. *Comm. Powder Diffr. Newsl.* **32**, 9-11 (2005).
54. Abràmoff, M. D., Magalhães, P. J. & Ram, S. J. Image processing with ImageJ. *Biophoton. Int.* **11**, 36-41 (2004).
55. Plimpton, S. Fast parallel algorithms for short-range molecular dynamics. *J. Comput. Phys.* **117**, 1-19 (1995).
56. Siu, S. W. I., Pluhackova, K. & Böckmann, R. A. Optimization of the OPLS-AA force field for long hydrocarbons. *J. Chem. Theory Comput.* **8**, 1459-1470 (2012).
57. Middleton, L. R. et al. Heterogeneous chain dynamics and aggregate lifetimes in precise acid-containing polyethylenes: experiments and simulations. *Macromolecules* **49**, 9176-9185 (2016).
58. Canongia Lopes, J. N., Pádua, A. A. H. & Shimizu, K. Molecular force field for ionic liquids IV: trialkylimidazolium and alkoxycarbonyl-imidazolium cations; alkylsulfonate and alkylsulfate anions. *J. Phys. Chem. B* **112**, 5039-5046 (2008).
59. Price, D. J. & Brooks, C. L. A modified TIP3P water potential for simulation with Ewald summation. *J. Chem. Phys.* **121**, 10096-10103 (2004).
60. Baaden, M., Burgard, M. & Wipff, G. TBP at the water− oil interface: the effect of TBP concentration and water acidity investigated by molecular dynamics simulations. *J. Phys. Chem. B* **105**, 11131-11141 (2001).

61. Hockney, R. W. & Eastwood, J. W. *Computer Simulation Using Particles* (Taylor & Francis, New York, NY, 1988).
62. Bolintineanu, D. S., Stevens, M. J. & Frischknecht, A. L. Atomistic simulations predict a surprising variety of morphologies in precise ionomers. *ACS Macro Lett.* **2**, 206-210 (2013).
63. Lueth, C. A., Bolintineanu, D. S., Stevens, M. J. & Frischknecht, A. L. Hydrogen-bonded aggregates in precise acid copolymers. *J. Chem. Phys.* **140**, 054902 (2014).
64. Bolintineanu, D. S., Stevens, M. J. & Frischknecht, A. L. Influence of cation type on ionic aggregates in precise ionomers. *Macromolecules* **46**, 5381-5392 (2013).
65. Brubach, J. B. *et al.* Performance of the AILES THz-infrared beamline at SOLEIL for high resolution spectroscopy. *AIP Conf. Proc.* **1214**, 81-84 (2010).
66. Roy, P., Rouzieres, M., Qi, Z. & Chubar, O. The AILES infrared beamline on the third generation synchrotron radiation facility SOLEIL. *Infrared Phys. Technol.* **49**, 139-146 (2006).
67. Bernardina, S. D. *et al.* New experimental set-ups for studying nanoconfined water on the AILES beamline at SOLEIL. *Vib. Spectrosc.* **75**, 154-161 (2014).
68. Voute, A. *et al*. New high-pressure/low-temperature set-up available at the AILES beamline. *Vib. Spectrosc.* **86**, 17-23 (2016).